Emergent properties of melanin-inspired peptide/RNA condensates

Amit Netzer[a], Itai Katzir[a], Avigail Baruch Leshem[a], Michal Weitman[b], and Ayala Lampel[a,c,d,e,1]

Most biocatalytic processes in eukaryotic cells are regulated by subcellular microenvironments such as membrane-bound or membraneless organelles. These natural compartmentalization systems have inspired the design of synthetic compartments composed of a variety of building blocks. Recently, the emerging field of liquid–liquid phase separation has facilitated the design of biomolecular condensates composed of proteins and nucleic acids, with controllable properties including polarity, diffusivity, surface tension, and encapsulation efficiency. However, utilizing phase-separated condensates as optical sensors has not yet been attempted. Here, we were inspired by the biosynthesis of melanin pigments, a key biocatalytic process that is regulated by compartmentalization in organelles, to design minimalistic biomolecular condensates with emergent optical properties. Melanins are ubiquitous pigment materials with a range of functionalities including photoprotection, coloration, and free radical scavenging activity. Their biosynthesis in the confined melanosomes involves oxidation-polymerization of tyrosine (Tyr), catalyzed by the enzyme tyrosinase. We have now developed condensates that are formed by an interaction between a Tyr-containing peptide and RNA and can serve as both microreactors and substrates for tyrosinase. Importantly, partitioning of Tyr into the condensates and subsequent oxidation-polymerization gives rise to unique optical properties including far-red fluorescence. We now demonstrate that individual condensates can serve as sensors to detect tyrosinase activity, with a limit of detection similar to that of synthetic fluorescent probes. This approach opens opportunities to utilize designer biomolecular condensates as diagnostic tools for various disorders involving abnormal enzymatic activity.

bioinspired materials | biomolecular condensates | liquid–liquid phase separation | peptide | melanin

Cells have evolved to provide subcellular controlled microenvironments or compartments that accommodate and control specific biocatalytic processes. Some of these compartments are membrane-bound and typically composed of lipid bilayers (1), whereas others are membraneless (2) and are formed by phase separation of proteins and nucleic acids. These natural compartments have inspired extensive efforts to design synthetic microreactors for a variety of purposes, including the increase of local substrate concentration in order to accelerate enzymatic reactions (3), facilitate small molecule synthesis (3), and deliver drugs or other therapeutic biomolecules (4, 5). Yet, the construction of synthetic microreactors typically requires the use of organic solvents and high-energy processes such as sonication, heating, or multiple extrusions, which might alter enzyme structure and activity. Moreover, some of the synthetic closed-compartment microreactors are limited in their permeability to reactants and enzymes, as well as in their capacity to release products, which limits their potential in biotechnological applications (6). Thus, there is still an unmet need to develop compartments with tunable properties that employ partitioning of client molecules, including enzymes, to control and regulate reactivity.

Recent advances with the potential to replace more traditional thermodynamically stable assemblies involve the development of compartments that mimic the properties of membraneless organelles (7–9). These build on insights regarding membraneless organelle formation by liquid–liquid phase separation (LLPS) of intrinsically disordered proteins (IDPs), either alone or in complexation with nucleic acids (10). The dynamic nature of compartments composed of IDPs or (poly)peptides with disordered domains (11–17) means that they can be designed to respond to specific stimuli (18–20) and enable the control of various properties, including polarity, diffusivity, surface tension, and recruitment of biomolecules (21). Despite these advantages, adapting phase-separated biomolecular condensates for specific applications, such as sensing, remains a challenge. Here, we were inspired by the ability of membraneless organelles to compartmentalize biochemical reactions and by the compartmentalized synthesis of melanin pigments in the

membrane-bound melanosomes. We then utilized features from both systems, to guide the development of minimalistic synthetic biomolecular condensates with properties that go beyond those of the biological counterparts.

Melanins are ubiquitous pigments (22) that have unique and protective properties including coloration (23, 24), broad UV–vis absorption (23, 25–27), electronic properties (28, 29), and free-radical (30) and metal-scavenging activity (31). In animals and humans, the brown-black eumelanin is formed during the late stages of the melanosome maturation by enzymatic oxidation-polymerization of tyrosine (Tyr), which is catalyzed by the enzyme tyrosinase (22). Unlike the laboratory-based bulk synthesis of melanin, the compartmentalization in the melanosome provides a means to spatio-temporally control Tyr oxidation-polymerization into melanin (32–34). Notably, the oxidized Tyr is thought to be bound to self-assembling proteins inside the melanosome, which provide a scaffold for melanin formation (35, 36). Inspired by the compartmentalized oxidation-polymerization of Tyr, which yields a pigment material with unique optical properties (37), we designed biomolecular condensates that acquire emergent optical properties following oxidation-polymerization by tyrosinase. The peptide/RNA condensates formed by LLPS of a short Tyr-containing peptide and RNA serve both as reactors, by encapsulating tyrosinase, and as precursors of the oxidation-polymerization reaction. Tyrosinase activation within the condensates confers unique optical properties including coloration, far-red UV–vis absorbance, and fluorescence. Importantly, since abnormal activity of tyrosinase is linked to various dermal disorders, monitoring the enzyme activity remains a major need. We now report that individual peptide/RNA condensates can be utilized as optical sensors to detect tyrosinase activity by a fluorescence response. Thus, this technology opens opportunities for biomedical applications and specifically for sensing applications of biocompatible condensates.

Results and Discussion

Inspired by melanin biosynthesis in cellular organelles, we sought to develop a multicomponent minimalistic compartmentalization system based on LLPS of a short Tyr-containing peptide and RNA (Fig. 1A). The resulting biomolecular condensate functions both as reaction centers, encapsulating tyrosinase, and as precursors of Tyr oxidation-polymerization. We hypothesized that oxidation–polymerization of the condensates should yield emergent optical properties in a confined peptide/RNA microenvironment (Fig. 1B).

We recently developed a library of minimalistic LLPS-promoting peptides that assemble into biomolecular condensates (38). We then focused on a minimalistic 9-mer sequence variant WGRGRGRWY (WGR). The peptide contains three glycine-arginine (Gly-Arg) dyad repeats that promote LLPS, two tryptophans, which promote π–π interactions, and a Tyr, which serves as the precursor for tyrosinase-catalyzed oxidation (Fig. 1A). We hypothesized that the Gly of the Gly-Arg dyads should promote flexibility, while the Arg promotes electrostatic interactions with RNA, as well as cation–π or π–π interactions (39) with the nucleobases or with the aromatic side chains of the peptide. As a model for RNA, we used polyuridylic acid polymer (poly-U), which is not prone to form a secondary structure and thus is accessible to interact electrostatically with the peptide (Fig. 1 A and B) (18, 39).

As the first step, we analyzed the LLPS propensity and formation of biomolecular condensates by complexation of the peptide and poly-U. For this purpose, we generated a phase diagram heat map by monitoring the turbidity of the sample in Tris-HCl buffer at pH 7.5, at 25 °C as a factor of peptide and poly-U concentration (Fig. 2A). Condensate formation was confirmed by optical and confocal microscopy (*SI Appendix,* Fig. S1 and Fig. 2B). We hypothesized that the main driving force of condensate formation is provided by electrostatic interactions between the positively
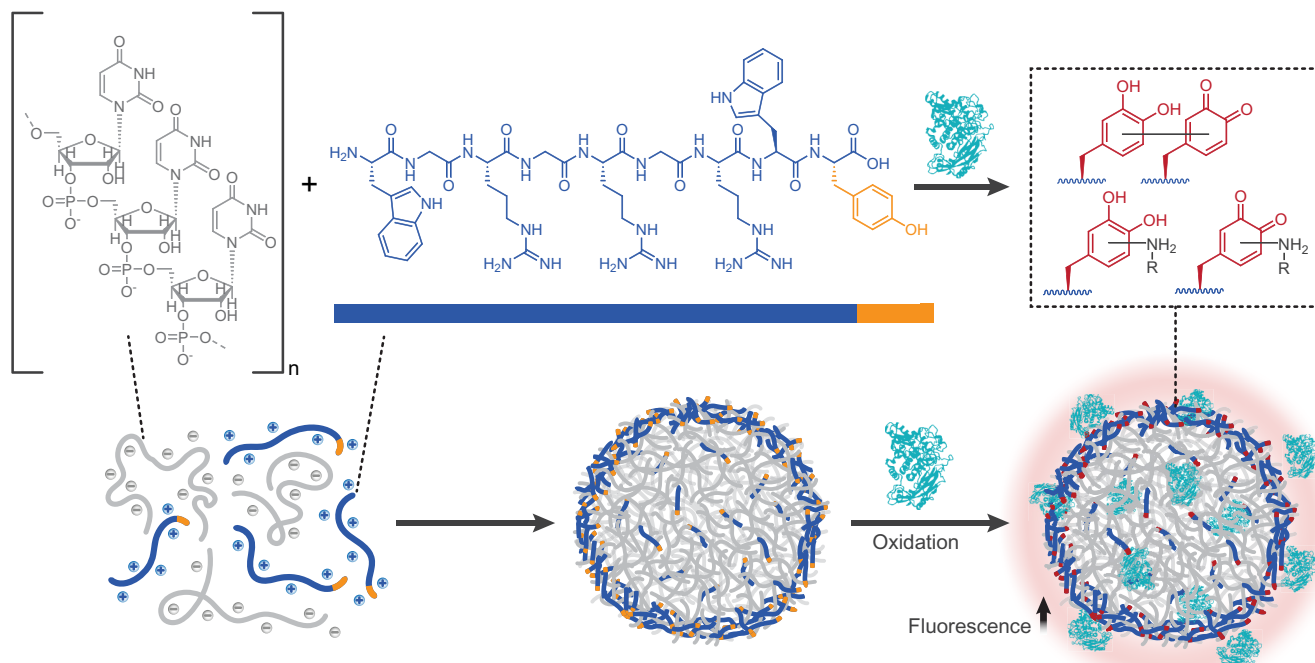
Fig. 1. Melanin-inspired peptide/RNA biomolecular condensates. *Top*: *Left* to *Right*: chemical structures of biomolecular condensate building blocks: poly-U (*Left*) and Tyr-containing peptide (WGRGRGRWY; WGR). Black dashed box: chemical structures of the side chain species (red) formed following tyrosinase (blue)-catalyzed oxidation–polymerization of the phenol side chain (yellow) within the condensates. *Bottom*: A schematic illustration of the system: biomolecular condensates formed by LLPS of the WGR peptide and RNA. Encapsulation of tyrosinase and subsequent oxidation–polymerization of the condensates results in an emerging far-red fluorescence, which is directly dependent on tyrosinase concentration and thus can serve as a reporting system for the detection of tyrosinase activity.

charged peptide and the negatively charged phosphate groups of poly-U. However, the phase diagram reveals a clear trend of condensate formation at a 2:1 ratio of basic:acidic groups, as calculated from the charge state of the peptide and poly-U (see *Materials and Methods* section). The average diameter of condensates formed by 2 mM peptide and 1 mg mL^{-1} poly-U is 5.04 ± 1.64 μm (*SI Appendix,* Fig. S1), as analyzed using optical microscopy (see Experimental section). Notably, confocal microscopy (Fig. 2*B*) and dynamic light scattering (DLS) estimation of the size distribution of condensates at the nanometer-low microscale (*SI Appendix,* Fig. S2) demonstrates that the diameter of the peptide/poly-U condensates can be regulated by changing the concentration of poly-U. Thus, the DLS analysis indicates that increasing the concentration of poly-U from 0.25 mg mL^{-1} to 1 mg mL^{-1} results in a shift in the average diameter of the condensates from 380 nm to 900 nm, respectively (*SI Appendix,* Fig. S2*A*).

The complexation of peptide and RNA and the organization of the resulting condensates were investigated by extensive confocal and electron microscopy analysis. For the confocal microscopy analysis, we hybridized FITC-labeled peptide (50 μM) and Cy3-oligoadenylate (Cy3-oligoA) with poly-U (18). The results revealed the formation of a core–shell architecture, with the peptide predominantly localized in the shell of the condensates, while the poly-U is uniformly distributed throughout (Fig. 2*C* and *SI Appendix,* Fig. S3). Varying the preparation method by i) mixing RNA stock solution in peptide stock solution or ii) dissolving peptide and RNA freeze-dried powders did not affect the core–shell architecture of the resultant condensates (*SI Appendix,* Fig. S4). The organization was further confirmed by transmission electron microscopy (TEM) analysis, which reveals a difference in the uranyl acetate electron absorption in the core and shell of

the condensates. The darker signal in the core is probably the result of stronger staining of the RNA by uranyl acetate (Fig. 2*D*). Interestingly, the TEM analysis also indicates adherence and partial fusion between condensates. Examining the fluorescence signal of the FITC-labeled peptide before and immediately after photobleaching, detected no fluorescence recovery after photobleaching (FRAP) over time (*SI Appendix,* Fig. S3 *A* and *B*). Given that the condensates are organized in a core–shell structure and that the peptide is mainly concentrated in the outer shell, we suspect that FRAP analysis of a labeled peptide might not reflect the diffusivity and dynamics of the condensate core. However, similar results from a second FRAP analysis using Cy3-oligoA (Fig. 2*E* and *SI Appendix,* Fig. S5*C*), as well as the findings from the TEM and confocal microscopy imaging, suggest that there is no diffusivity of peptide or RNA molecules in the condensates. Moreover, treating the condensates with 0.5 M NaCl does not alter the turbidity of the condensates (*SI Appendix,* Fig. S6). Thus, we can conclude that the peptide/RNA condensates are not liquid assemblies and are not formed by a typical LLPS process like membraneless organelles, nor by classical complex coacervation, driven by electrostatic interactions between anionic and cationic building blocks. Instead, the findings suggest that, in addition to electrostatic interactions between the cationic peptide and the poly-U, the dense shell of the condensates is formed by peptide–peptide interactions. The intermolecular contacts between the peptide building blocks may be mediated by π–π interactions between Arg and the aromatic side chains and by π–π stacking between the aromatic side chains. These interactions can also explain the trend seen in the phase diagram, where condensates are formed at a 2:1, rather than a 1:1 ratio of basic:acidic groups. Notably, these peptide–peptide interactions do not result in formation of a specific
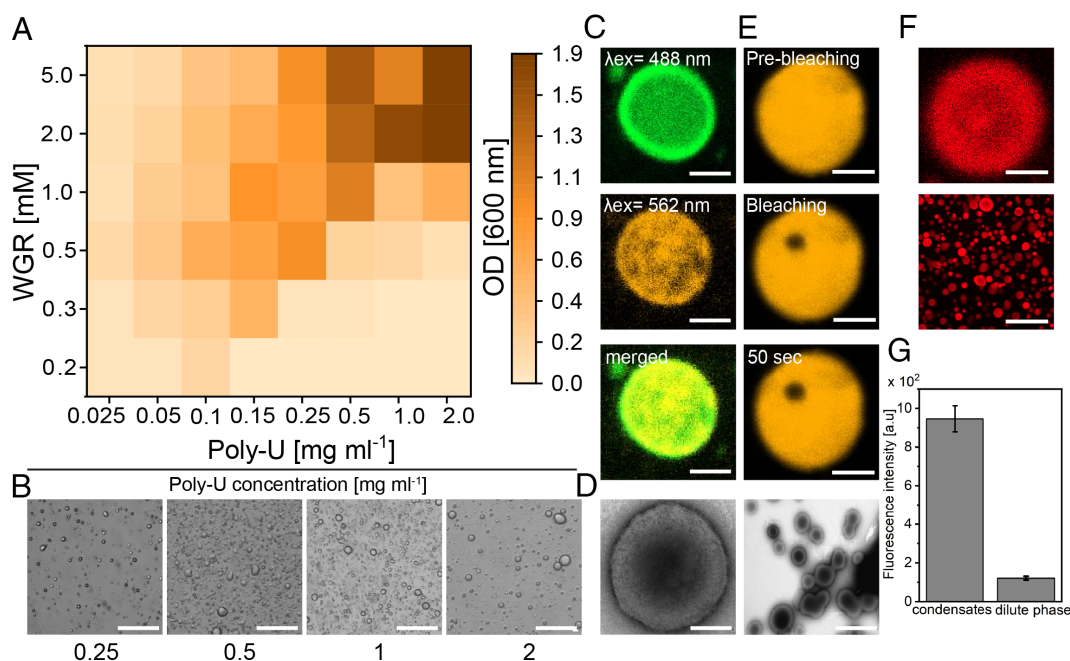

Fig. 2. LLPS propensity and organization of peptide/RNA biomolecular condensates. (*A*) Phase diagram heat map of peptide/RNA LLPS as a function of peptide and poly-U concentration, measured by turbidity assay. (*B*) Confocal microscopy transmitted light images of condensates formed by LLPS of WGR (2 mM) with increasing concentrations of poly-U in 10 mM Tris-HCl buffer pH 7.5 at 25 °C. (*C*) Confocal microscopy images of condensates formed by peptide/RNA (2 mM/1 mg mL^{-1}) with FITC-labeled peptide (50 μM, λ_{ex} = 488 nm) and Cy3-oligoA (0.012 μM, λ_{ex} = 562 nm) showing core–shell organization. Images show the z-stacking middle section. (*D*) TEM images of the peptide/RNA condensates showing a condensed shell. [Scale bars, 100 nm (*Left* image), 1 μm (*Right* image).] (*E*) Confocal microscopy FRAP analysis images of peptide/RNA condensates (1 mM/0.5 mg mL^{-1}) before and after photobleaching of Cy3-oligoA (0.012 μM) showing no recovery of fluorescent signal. (*F*) Confocal microscopy images of Atto633-tyrosinase (0.06 mg mL^{-1}; λ_{ex} = 640 nm) encapsulation in peptide/RNA (2 mM/1 mg mL^{-1}) condensates. (*G*) Atto633-tyrosinase fluorescence in condensates compared to the dilute phase measured by confocal microscopy analysis. Values represent an average of 8 droplets, SEs are indicated. Confocal microscopy scale bars, 5 μm (panel *C*, *E*); 20 μm (panel *B* and *F*, *Bottom* image).

secondary structure, since circular dichroism (CD) analysis, reveals that the peptide remains in a random coil conformation under LLPS conditions (*SI Appendix*, Fig. S7).

As the next step, we studied the partitioning of tyrosinase in the peptide/RNA condensates by labeling the enzyme with Atto633 and using laser scanning confocal microscopy to compare the partitioning (0.3 mg mL^{-1}) in the condensates and in the surrounding phase. As shown in Fig. 2 *F* and *G*, tyrosinase partitions preferentially into the peptide/RNA condensates, with the Atto633-tyrosinase fluorescence intensity 7.8-fold higher in the condensates than the surrounding phase, and predominantly localized to the condensed shell with slow mobility (23.6% recovery of FRAP, *SI Appendix*, Fig. S8). Interestingly, the localization and distribution of enzyme in peptide/RNA condensates are affected by the order of reactant addition and mixing the enzyme with the RNA solution before initiation of condensate formation results in a mostly homogenous distribution of the enzyme in the condensates (*SI Appendix*, Fig. S9). To study the effect of the labeling dye, we compared the localization of enzyme labeled with Atto633 or Atto550, which have LogP values of 1.41 vs. 3.73, respectively. The results indicate that Atto550-labeled tyrosinase is distributed in heterogeneous clumps in the peptide/RNA condensates and not only in the condensate shell (*SI Appendix*, Fig. S10). These clumps might be the result of interactions between the hydrophobic dye and the peptide, or due to aggregation of the dye in the condensed phase.

The encapsulation efficiency (EE%) of the enzyme is 92.06 ± 0.01%, as calculated by measuring the enzyme concentration in the dilute phase (supernatant) by absorbance spectroscopy following centrifugation of enzyme-loaded condensates (see Experimental section).

UV–vis spectroscopy was used to analyze the optical properties of the peptide/RNA condensates following oxidation by encapsulated tyrosinase. To exclude the contribution of scattering following oxidation, we subtracted the spectra of unoxidized condensates from those of oxidized material (*SI Appendix*, Fig. S11), which yielded spectra similar to those acquired using an integrating sphere (*SI Appendix*, Fig. S12). In addition, we monitored the absorbance of peptide/RNA (2 mM/1 mg mL^{-1}) condensates over time during oxidation. Reactions were performed in 10 mM Tris-HCl buffer at pH 7.5, and 25 °C. The intensity of a broad absorbance with λ_{max} = ~500 nm, observed immediately upon the addition of tyrosinase (t$_{5\ min}$), increases after 1 h of oxidation (t$_{1h}$), and a second maximum at λ = 400 nm emerges at t$_{2h}$. This peak continued to increase and was joined at t$_{3h}$, by a far-red absorbance at λ_{max} = 632 nm, which increases in intensity at t$_{5h-6h}$. After 24 h (t$_{24h}$), the λ_{max} = 400 nm absorbance blue-shifts to λ_{max} = 362 nm and the intensity of the λ_{max} = 632 nm peak increases further (Fig. 3*A*). Raising the reaction temperature from 25 °C to a physiological temperature (37 °C) increases the far-red absorbance, which is observed in the condensate after 1 h of oxidation and reaches a high intensity (OD = >0.5) after 3 h (Fig. 3*C*). We compared the UV–vis absorbance of the oxidized condensates to that of oxidized peptide in the absence of RNA, which does not form condensates (Fig. 3*B*). There was no λ_{max} = 632 nm absorbance when the peptide was oxidized at 25 °C (Fig. 3*B*) or 37 °C (*SI Appendix*, Figs. S13 and S14). Instead, there is a broad absorption with a maximum at around 500 nm. Over oxidation time, the intensity of the λ_{max} = 500 nm maximum decreases and the absorption becomes broader (Fig. 3*B* and *SI Appendix*, Fig. S13) and resembles that of natural melanin (*SI Appendix*, Fig. S15). Similarly, the UV–Vis absorption of peptide that was preoxidized for 1 h or 24 h at 25 °C and subsequently mixed with poly-U does not exhibit the λ_{max} = 632 nm absorbance but rather a λ_{max} = 500

nm maximum at a short oxidation time and a broadband absorption after 24 h of oxidation (*SI Appendix*, Fig. S16). To investigate whether the λ_{max} = 632 nm absorption is mediated by noncovalent interactions or by newly formed polymers, we analyzed the UV–Vis absorbance of oxidized condensates following the addition of 1.8 M urea, which is expected to promote dissociation of H-bonding interactions. As observed in *SI Appendix*, Fig. S16, the addition of urea does not significantly affect the far-red absorption (*SI Appendix*, Fig. S17). In addition, we analyzed the optical properties of oxidized condensates following heating at 70 °C (for 1 h). The heating results in the production of a sediment that contains condensates alongside spherical aggregates, which broadly absorb at λ = 640 nm and fluoresce upon excitation at λ = 632 nm (*SI Appendix*, Fig. S18). These results imply that the far-red absorbance of the oxidized condensates can be attributed to a conjugated system that is formed exclusively in the condensate microenvironment, rather than to oxidation of soluble peptide. Notably, oxidation of short self-assembling peptides was previously reported to result in peptide polymerization, presumably through conjugation of the terminal amine group with the oxidized Tyr (27, 40). To study the role of the RNA in the system, we analyzed the optical properties of homotypic condensates formed by simple coacervation of the WGR peptide, in the absence of RNA. The results indicate that like the heterotypic peptide/RNA condensates, homotypic condensates exhibit the λ_{max} = 632 nm absorbance maximum after 3 h of oxidation by tyrosinase at 37 °C (*SI Appendix*, Fig. S19). This suggests that the condensation of the peptide into peptide/RNA condensates is a prerequisite for the emergent optical properties, and that the peptide, rather than the RNA, undergoes oxidation–polymerization.

To confirm that the WGR peptide is indeed oxidized by tyrosinase and to gain insights into the oxidation–polymerization mechanism, we performed a kinetics LC-MS (Liquid chromatography-mass spectrometry)/MS analysis. For this purpose, we oxidized WGR peptide at a final concentration of 2 mM in Tris-HCl buffer at pH 7.5 using tyrosinase (0.2 mg mL^{-1}) at 25 °C. The characteristic peptide signals [597.3070 (z = 2) -> 507.2603] were assessed at initiation of oxidation 0 h, and at 4 h, and 24 h (Fig. 3*D* and *SI Appendix*, Fig. S20). At t$_{0h}$, a major signal of the peptide is observed (1.1 min) along with a new species with a mass of 1204.5636 (1.75 min). Accurate mass high-resolution analysis detects a mass change of 11.9627 Da in the latter, which can be attributed to the addition of one oxygen and a reduction of 4 hydrogens. This finding is consistent with the recently reported polymerization and condensation mechanism of Tyr by tyrosinase (25) and corresponds to the Raper–Mason pathway (25). The observed product indicates that the three-step oxidation sequence (WGR+O-2H-2H) is extremely fast and occurs immediately upon tyrosinase addition. At t$_{0h}$, two more species appear: WGR with the addition of oxygen (WGR+O) and addition of oxygen along with reduction of two hydrogens (WGR+O-2H). After 4 h of oxidation, a variety of new species with higher mass properties appear on the chromatogram, while the starting material is still present but at a lower concentration (Fig. 3*D*). Finally, after 24 h of oxidation, the WGR peptide signal disappears and is replaced by new peaks that might represent the polymerized peptide (*SI Appendix*, Fig. S20). SDS PAGE analysis detects a new band with a higher mass than that of unoxidized condensates following oxidation of peptide/RNA condensates, which probably represents a polymeric species (*SI Appendix*, Fig. S21).

These changes are reflected in the appearance of the reaction before and after addition of tyrosinase and over oxidation time, where the initially translucent peptide solution becomes opaque following addition of RNA and formation of condensates. Five
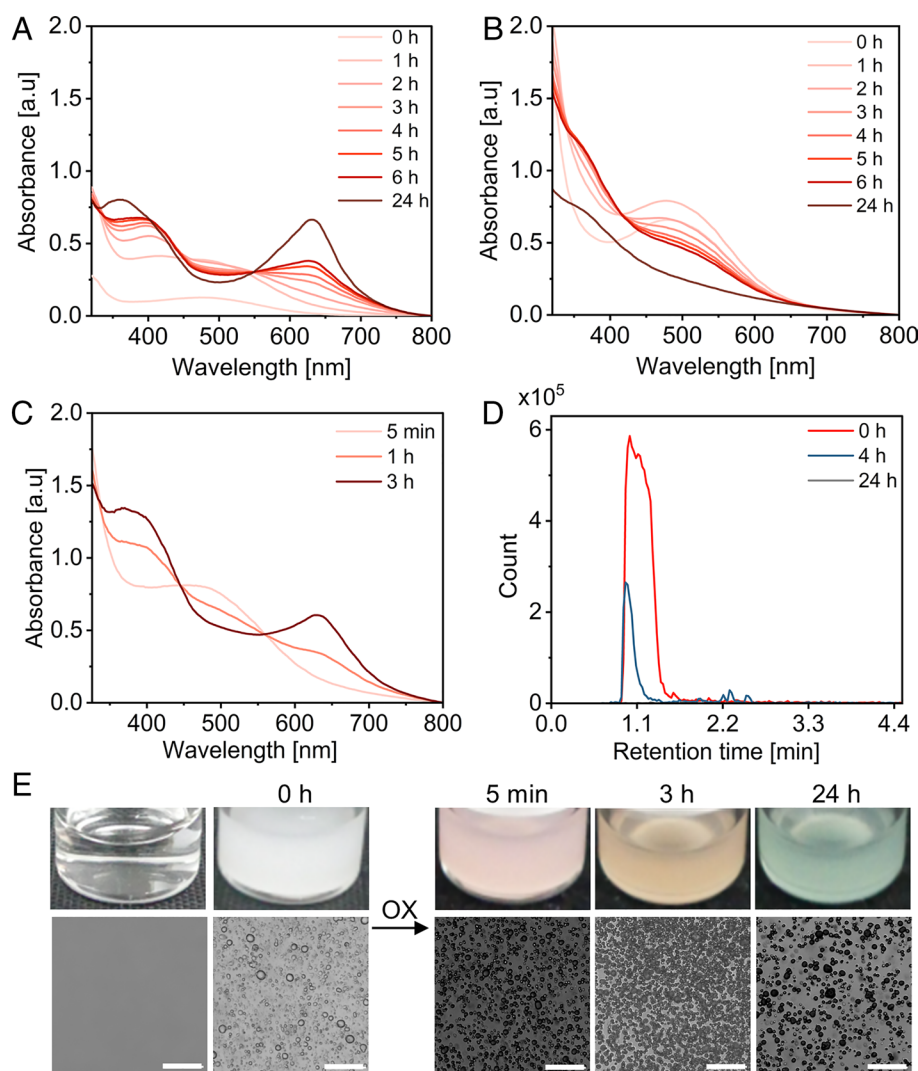
Fig. 3. Melanin-inspired biomolecular condensates have unique far-red absorbance following oxidation. (*A* and *B*) UV–vis absorbance spectra of (*A*) peptide/RNA condensates (2 mM/1 mg mL^{-1}) or (*B*) peptide in the absence of RNA (2 mM, no condensates) over increasing oxidation time at 25 °C. (*C*) UV–vis absorbance spectra of peptide/RNA condensates performed at 37 °C. (*D*) Extracted ion chromatography (EIC) of peptide (2 mM) oxidation over time (0 min, 4 h, and 24 h of oxidation) showing the disappearance of the peptide peak with oxidation. (*E*) Macroscopic (*Top*) and confocal microscopy transmitted light images (*Bottom*) of (from *Left* to *Right*): peptide alone (clear solution), peptide/RNA condensates before (*Left*) and after (*Right*) oxidation. (Scale bars, 20 μm.)

minutes after tyrosinase addition, the reaction becomes pink and then changes to orange after 6 h of oxidation due to increased oxidation and polymerization, and then, a green color appears after 24 h (Fig. 3 *E*, *Top*). In contrast, the color of an oxidized peptide solution that does not form condensates shifts from strong red to orange and eventually to yellow (*SI Appendix*, Fig. S14).

Confocal and optical microscopy imaging of condensate abundance over time revealed that the oxidized condensates remain stable after 24 h (Fig. 3 *E*, *Bottom* and *SI Appendix*, Fig. S22, *Top*) while unoxidized condensates are not observed after 1 h (*SI Appendix*, Fig. S22, *Bottom*). Recent reports that H-bonding interactions of dopa-mediated LLPS suggest that the stability of oxidized condensates might be mediated by H-bonding interactions of oxidized phenols (41, 42).

The emergent optical properties of individual condensates following oxidation were investigated by using real-time confocal microscopy at $\lambda_{ex} = 405$ nm and $\lambda_{ex} = 640$ nm to monitor the intrinsic fluorescence of peptide/RNA condensates over 72 h of oxidation at 25 °C by. As shown in Fig. 4 *A–C*, the fluorescence intensity of the condensates increases over oxidation time and reaches a plateau after 24 h. These findings, together with the LC-MS/MS analysis, suggest that the emergent fluorescence is due to the formation of a polymerized peptide network in the condensates. A similar emission with $\lambda_{ex} = 396$ nm and 628 nm is observed by fluorescence spectroscopy of oxidized condensates in bulk (*SI Appendix*, Fig. S23). This is in accordance with the far-red emission previously reported for polymeric peptide particles that are formed by oxidation of a Tyr-containing short peptide, following addition and reactive incorporation of Phe to the oxidized Tyr side chain (27). In addition, a recent paper described phase-separated condensates that are formed by a Tyr-peptide conjugated to a polymeric linker and subsequently reorganize into a semipermeable core–shell architecture upon oxidation of Tyr to di-Tyr by HRP at the interface of the condensate and the dilute phase (43). In contrast, the two oxidation steps catalyzed by tyrosinase mean that the emergent emissions of the peptide/RNA condensates are a result of a highly efficient partitioning of tyrosinase, oxidation, and subsequent polymerization of the Tyr side chain within the peptide building block.

Based on these results, we sought to utilize the emergent fluorescence of the condensates as a reporting system for the detection of tyrosinase activity. Treating the peptide/RNA condensates with varying concentrations of tyrosinase between 0.005 and 0.5 mg mL^{-1} at 37 °C for 3 h revealed a positive relationship between the absorbance of the condensate samples and increasing tyrosinase concentrations (*SI Appendix*, Fig. S24). We then monitored the fluorescence response of peptide/RNA condensates (2 mM/1 mg mL^{-1}) to different concentrations of tyrosinase at a physiological temperature (37 °C). Fluorescence at both $\lambda_{ex} = 405$ nm and at $\lambda_{ex} = 640$ nm was measured 10 min after enzyme addition using confocal microscopy. As shown in Fig. 4*D* and *SI Appendix*, Fig. S25, the fluorescence intensity of condensates increases with increasing tyrosinase concentration in a dose-dependent manner, with a linear detection region
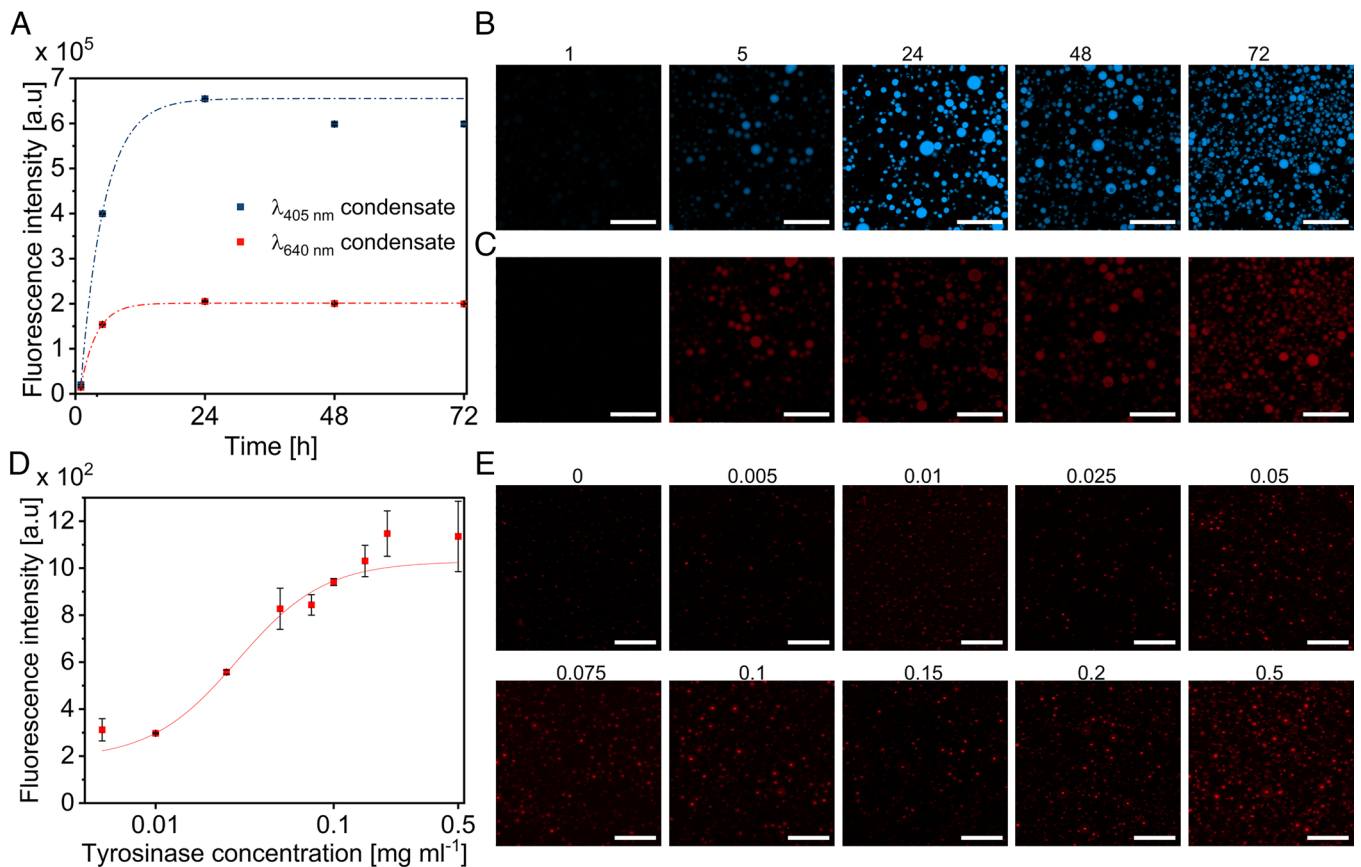
Fig. 4. Emergent fluorescence of individual biomolecular condensates can be utilized for tyrosinase detection. (*A*–*C*) Fluorescence intensity (*A*) and images (*B* and *C*) of peptide/poly-U condensates (2 mM/1 mg mL^{-1}) following oxidation (0.2 mg mL^{-1} tyrosinase) over time (1 h to 72 h) at 25 °C measured by confocal microscopy. Images were acquired at λ_{ex} = 405 nm (*B*) or λ_{ex} = 640 nm (*C*). (*D* and *E*) Fluorescence intensity (*D*) and confocal microscopy images (*E*) of peptide/poly-U condensates (2 mM/1 mg mL^{-1}) treated with varying concentrations of tyrosinase (0.005, 0.01, 0.025, 0.05, 0.075, 0.1, 0.15, 0.2, and 0.5 mg mL^{-1}) acquired at λ_{ex} = 640. For (*A*) and (*D*): values represent an average of 8 condensates (*A*) or 10 condensates (*D*), SEs represent SD of 3 independent measurements. Signal of the dilute phase was subtracted. (Scale bars for *B*, *C*, *E*, 20 μm.)

between tyrosinase concentration of 0.025 to 0.1 mg mL^{-1}. The limit of detection (LOD) of the condensate reporting system was calculated by fitting a four-parameter logistic regression with a zero base-line. This provided a four-parameters fit:

$$y = A2 + \frac{A1 - A2}{\left(1 + \left(\frac{x}{x1/2}\right)^p\right)}, \text{ where A1 and A2 are the initial and}$$

final values of fluorescence intensity, respectively, x is the tyrosinase concentration, $x_{1/2}$ is the tyrosinase concentration which results in 50% fluorescence response, and p is the power (the fit parameters are summarized in the Experimental section). The results yield an LOD of 0.011 mg mL^{-1} using λ_{ex} = 405 nm, and 0.0058 mg mL^{-1} using λ_{ex} = 640 nm. These LOD values are similar to the reported ones of phenolic small-molecule substrates used as fluorescence probes for tyrosinase activity detection (44).

Conclusions

Abnormal activity of tyrosinase is related, either directly or indirectly, to a range of pathologies: inactive enzyme leads to albinism, while higher-than normal activity results in hyperpigmentation (45) and can also lead to malignant melanoma (46). Thus, developing biocompatible systems for the detection of tyrosinase activity in situ under physiological conditions is crucial for the diagnosis of dermal disorders. Inspired by the compartmentalization of melanin synthesis, we developed peptide/RNA biomolecular condensates that act as compartments for tyrosinase encapsulation and precursors for tyrosinase oxidation. These condensates remain stable and intact

following peptide oxidation–polymerization and acquire optical properties including green coloration, far-red absorbance, and fluorescence that exceed those of natural melanin. Moreover, we show that individual condensates can be used as robust long-term (days) sensors for detection of tyrosinase activity at physiological temperatures. Thus, the designed biomolecular condensate platform opens opportunities for applications as a diagnostic tool of dermal disorders. In a broader sense, the presented approach could be used for a wide variety of sensing applications by designing biomolecular condensates that serve as microreactor/precursors of specific enzymes of interest.

Materials and Methods

Materials. Peptides were custom synthesized and purified (95% purity) by Genscript, Hong Kong. Unless otherwise specified, all reagents were of the highest available purity. Polyuridylic acid (poly-U), tyrosinase from mushroom, Atto 633 and Atto 550 protein labeling kits, Trizma base, Tricine, and sodium dodecyl sulfate (SDS) were purchased from Sigma. Fifteen bases Cy3-oligoA was purchased from IDT. NaOH and HCl were purchased from BioLab. In addition, 16.5% Mini-PROTEAN Tris-Tricine Gel, Precision Plus Protein Dual Xtra Prestained Protein Standards and Tricine Sample Buffer for Protein Gels, were purchased from BIO-RAD. Bovine Serum Albumin (BSA) Fraction V was purchased from MP Biomedical.

Phase Diagram and Turbidity Measurements. Condensates were prepared by mixing a stock solution of peptide (10 mM) dissolved in 10 mM Tris-HCl buffer pH 7.5 (solution A) with a stock solution of 19.85 mg mL^{-1} poly-U dissolved in ultrapure water (solution B). Condensates were formed immediately upon adding

solution B to solution A. The peptide and poly-U stock solutions were prepared at final concentrations of 0.2, 0.3, 0.5, 1, 2, and 5 mM (peptide) and 0.025, 0.05, 0.1, 0.15, 0.25, 0.5, and 1 mg mL^{-1} (poly-U), in a total volume of 150 µL. Turbidity was immediately visible upon addition of poly-U, which initiates phase separation. UV–vis absorbance spectra were measured in a 384-well plate by a Synergy H1 microplate reader, under 30 s shaking before each measurement. A phase diagram heat map was based on turbidity measured at λ = 600 nm. All experiments were performed in triplicates.

The positive:negative charge ratio of peptide:poly-U was calculated as the WGR peptide charge state is +3. The charge of the poly-U was calculated as 306.2 g mol^{-1} based on the MW of the monomeric unit of the polymer (MW of UMP subtracted by the MW of the leaving water molecule during the polymerization process).

Optical Microscopy. Samples of peptide and poly-U at varying concentrations were prepared as indicated for each optical microscopy analysis. For analyzing condensate diameter, samples were prepared at a final peptide concentration of 2 mM and 1 mg mL^{-1} of poly-U. The average diameter of the condensates was calculated from measurements of 23 condensates, and the SD is presented. Samples were analyzed by visualization in a clear glass bottom 384-well plate by an inverted optical microscope (OPTIKA Microscopes Italy) equipped with X-LED 8 W lamp and 60× objective.

DLS Analysis. Peptide/RNA condensates were prepared with either 2 mM peptide and varying poly-U concentrations (0.25, 0.5, and 1 mg mL^{-1}) or with 0.5 mg mL^{-1} poly-U and varying peptide concentrations (1, 2, and 5 mM) in 10 mM of Tris-HCl buffer at pH 7.5 at 25 °C. Each sample (75 µL) was placed in a disposable plastic microcuvette (purchased from Golik). The diameter of the condensates was calculated as the average of 14 repeats.

CD Analysis. WGR peptide and poly-U were analyzed at final concentrations of 1 mM and 0.5 mg mL^{-1}, respectively, in 10 mM of Tris-HCl buffer at pH 7.5 and samples were placed in a 0.1 mm path length quartz cuvette (purchased from ISI) at 25 °C. Spectra were acquired over a range of 190 to 260 nm using a Chirascan spectrometer (Applied Photophysics). Background (buffer) values were subtracted from all CD spectra. All measurements were performed in triplicate.

Confocal Microscopy Imaging. Condensates were imaged using a laser scanning confocal microscope (Zeiss LSM 900 inverted microscope), x20/0.8 NA Plan-Apochromat objective. Images were collected and processed using Zen software (Zeiss). Bright-field images were obtained by a PMT channel using a 405-nm laser. Fluorescence images were recorded using 488, 561, and 640-nm lasers for FITC, Cy-3, and Atto 633, respectively. Fluorescence intensity in the condensates was analyzed using Zen software (Zeiss).

To test how different preparation protocols affect the condensate architecture, the peptide was dissolved in buffer and the pH was adjusted to 7.5. The dissolved peptide was freeze-dried, and the dissolved poly-U was also freeze-dried. The freeze-dried peptide and poly-U powders were mixed and then redissolved in water.

FRAP. FRAP experiments were performed using a Zeiss LSM 900 inverted microscope as described above. Peptide/RNA condensates were prepared at a final concentration of 2 mM/1 mg mL^{-1} with FITC-labeled peptide (50 µM, λ_{ex} = 488 nm) or Cy3-oligoA at final concentration of 0.012 µM. All solutions were prepared in 10 mM Tris-HCl buffer pH 7.5 at 25 °C. A circular area with radius of 1 µm was bleached using 10 iterations with 488/561/640 nm lasers for FITC/Cy3/Atto-633, respectively, at 100% intensity; subsequent recovery of the bleached area was recorded by either a 488 nm or 561 nm laser. Photobleaching correction and recovery time were calculated using OriginLab. The final FRAP recovery curve represents an average of the results with five individual condensates. For photobleaching correction, the emission intensity at the region of interest before photobleaching was set as the maximum (100% recovery) and the intensity immediately after photobleaching as the minimum (0% recovery).

TEM. Peptide/RNA condensates were prepared at a final concentration of 2 mM and 1 mg mL^{-1} for the peptide and poly-U, respectively, in 10 mM Tris-HCl buffer pH 7.5 at 25 °C. An aliquot of 10 µL of the sample solution was applied to a carbon-coated grid and incubated for 2 min. Excess solution was removed by blotting the grid with a piece of filter paper, followed by staining with 10 µL of 2% (w/v) uranyl acetate solution for 2 min. After blotting excess stain solution,

the grid was left to air-dry. The negatively stained sample was imaged by a JEM-1400Plus TEM operating at 80 kV. Images were recorded using a SIS Megaview III camera, iTEM imaging platform (Olympus).

Tyrosinase Labelling. Tyrosinase from mushrooms (Sigma-Aldrich) was labeled on the amines, using a succinimidyl ester functionalized Atto633 or Atto550 protein labeling kit (Sigma-Aldrich). The labeled enzyme was purified using a gel filtration column that was received with the kit. The labeled-tyrosinase solution concentration was determined spectroscopically. The LogP values of Atto633 and Atto550 were calculated using Molinspiration software.

Encapsulation Efficiency of Atto 633-Labeled Tyrosinase. Stock solutions (0.6 mg mL^{-1}) of tyrosinase labeled with Atto 633 were prepared as described above. Condensate solutions with final concentrations of 2 mM peptide and 1 mg mL^{-1} poly-U of were prepared in 10 mM Tris-HCl pH 7.5 at 25 °C. Tyrosinase (final concentration of 0.3 mg mL^{-1}) was added to the peptide/RNA condensates. After 10 min incubation, samples were centrifuged at 15,000 rcf for 10 min. A volume of 120 µL supernatant was collected and vortexed. Absorbance was measured in a 384-well black plate by a Biotek H1 synergy plate reader. All experiments were performed in triplicate. The concentration in the supernatant was determined from calibration curves of Atto633-tyrosinase. The encapsulation efficiency was calculated according to Eq. **1**:

$$\% \, EE = \left(\frac{C_T - C_{sup}}{C_T} \right) * 100. \qquad [1]$$

UV–Vis Spectroscopy. Peptide/RNA condensates were prepared using 2 mM peptide and 1 mg mL^{-1} poly-U in 10 mM Tris-HCl at pH 7.5. Tyrosinase was added to the condensates to give a final concentration of 0.2 mg mL^{-1} for 25 °C incubation and 0.005, 0.01, 0.025, 0.05, 0.075, 0.1, 0.15, 0.2, and 0.5 mg mL^{-1} for 37 °C incubation. Simple coacervation samples of WGR peptide were prepared using 20 mM peptide in 10 mM Tris-HCl, 0.2 M NaCl at pH 8. Tyrosinase was added to samples of condensates to give a final concentration of 0.2 mg mL^{-1} and incubated at 37 °C for 3 h. The saturated dissolved oxygen content is 8.24 mg L^{-1} and 6.71 mg L^{-1} at 25 °C and 37 °C, respectively. Sepia melanin solution was prepared by dissolving 1.2 mg mL^{-1} of Sepia officinalis melanin (Sigma) in 1 M NaOH. After overnight sonication, the solution was diluted by 50% v/v in 20 mM Tris buffer. The pH was adjusted to a value of 7.5 by adding 1 M HCl solution and then 20 mM Tris buffer was added to obtain a final Sepia melanin concentration of 0.36 mg mL^{-1} (equivalent to the concentration of Tyr in the oxidation experiments). UV–vis spectra of the samples between 280 nm and 800 nm were obtained at the indicated oxidation times by using a Biotek H1 synergy plate reader. The spectra presented in *SI Appendix*, Fig. S11 were acquired using a UV 2600 Shimadzu UV-VIS recording spectrophotometer equipped with an ISR-2600 PLUS integrating sphere. A blank spectrum of Tris-HCl buffer pH 7.5 was subtracted from all spectra. All spectra represent the average of triplicates. Data from the 37 °C incubations were fitted to a three-parameter exponential-asymptotic equation (Eq. **2**) where *a* is the asymptote, *b* is the response range, and *c* is the rate (Table 1).

$$y = a - b * c^x. \qquad [2]$$

Fluorescence Spectroscopy. Emission spectra of 45 µL of oxidized peptide/poly-U condensate samples (2 mM/1 mg mL^{-1}) were obtained with a Horiba Jobin Yvon FL3-11 spectrofluorometer, using a quartz cuvette with path length of 3 mm. Data were analyzed using OriginLab. Measurements were performed in triplicate.

LCMS/MS. LC-MS of Tyr oxidation was obtained with a 6545 QTOF mass spectrometer, which was equipped with an electrospray ionization interface coupled to a 1260 UHPLC, a G4204A quaternary pump, G4226A ALS auto-sampler, and

Table 1. Exponential fitting, asymptotic

a	0.734 ± 0.076
b	0.757 ± 0.070
c	0.00016 ± 0.00035
R-square (COD)	0.987
Adj. R-square	0.983

G1316C thermostatted column compartment (purchased from Agilent technologies). UHPLC was carried out on an Aeris TM widepore XB-C18, 100Å, 100 x 2.1 mm, 3.6 μm column (purchased from Agilent technologies), with a water (1% formic acid)-acetonitrile gradient elution, from 5 to 80% acetonitrile for 12 min at a flow rate of 1.5 mL/min. Duplicate 5 μL samples were injected into the LC-MS/MS instrument, and an average peak area of three analyses was calculated. Detection of WGR was monitored by the ion transitions 597.307 m/z [M + 2H, Z = 2] 2+ → 507.2603 [M + 2H, Z = 2] 2+ m/z collision energy for product ion mode (MS/MS) 37 V. The source temperature was set to 300 °C, Fragmentor 250 V, drying gas 8 L/min, nebulizer 40 psi, sheath gas temperature 400 °C, sheath gas flow 12 L/min, ion spray voltage was 4.5 kV, and nozzle voltage 1,500 V.

SDS PAGE Analysis. Peptide solution was prepared at a final concentration of 2 mM, Peptide/RNA condensates were prepared at a final concentration of 2 mM and 1 mg mL^{-1} for the peptide and poly-U, respectively. Oxidized peptide/RNA condensates were prepared at a final concentration of 2 mM, 1 mg mL^{-1}, and 0.2 mg mL^{-1} of the peptide, poly-U, and tyrosinase, respectively. Treated oxidized peptide/RNA condensates were sonicated at 70 °C for 1 h. The samples were prepared in 10 mM of Tris-HCl buffer pH 7.5 and were incubated at 37 °C for 3 h, before being diluted threefold and loaded to the Tris Tricine SDS gel (16.5%). Control protein BSA was prepared to a final concentration of 1 mg mL^{-1}. All samples were loaded after mixing 16 μL of the samples with 4 μL of Tris-Tricine sample buffer. Running voltage was 140 V.

Confocal Microscopy Analysis of Condensates Fluorescence Following Oxidation. Peptide/poly-U condensates (2 mM/1 mg mL^{-1}) were oxidized at 25 °C at pH 7.5 by 0.2 mg mL^{-1} of tyrosinase. The fluorescence intensity inside condensates and in the dilute phase was measured over 72 h at either λ$_{ex}$ = 405 nm or λ$_{ex}$ = 640 nm. The background given by the dilute phase was subtracted from the condensate absorbance. Each data point represents an average of 8 condensates. Data were fitted to a three-parameter exponential-asymptotic equation (Eq. **2**) (Table 2).

Confocal Microscopy Analysis of Condensate Fluorescence at Varying Tyrosinase Concentrations. Varying concentrations of tyrosinase (0.005, 0.01, 0.025, 0.05, 0.075, 0.1, 0.15, 0.2, and 0.5 mg mL^{-1}) were added to

Table 2. Exponential fitting, asymptotic

	λ$_{ex}$ = 405 nm	λ$_{ex}$ = 640 nm
a	65,518.487 ± 903.948	20,127.142 ± 165.824
b	79,853.044 ± 1,838.605	26,314.524 ± 320.202
c	0.795 ± 0.019	0.700 ± 0.009
R-square (COD)	0.99966	0.99988
Adj. R-square	0.99931	0.99975

Table 3. Sigmoidal fitting, linear regression

	λ$_{ex}$ = 405 nm	λ$_{ex}$ = 640 nm
A1	369.021 ± 161.374	205.313 ± 93.237
A2	6,995.859 ± 50.348	1,007.105 ± 86.371
x$_{1/2}$	0.042 ± 0.025	0.028 ± 0.001
p	3.275 ± 1.857	1.942 ± 0.878
R-Square (COD)	0.99998	0.99717
Adj. R-Square	0.99998	0.99548

peptide/RNA condensates (2 mM/1 mg mL^{-1}) at pH 7.5 and 37 °C. Each sample was imaged using a laser scanning confocal microscope (as described above) at either λ$_{ex}$ = 405 nm or λ$_{ex}$ = 640 nm following 10 min incubation with the enzyme. Each data point represents the average of 10 condensates, and SDs are presented. The data were fitted to a four-parameter logistic regression with iteration algorithm of Orthogonal Distance Regression and Levenberg Marquardt for λ$_{ex}$ = 405 nm and λ$_{ex}$ = 640 nm, respectively (Eq. **3**). *A1* and *A2* are the initial and final fluorescence intensity, respectively, *x* is the tyrosinase concentration, *x$_{1/2}$* is the *x* value that results in a 50% fluorescence intensity response, and p is the power. The LOD was calculated as the initial value (*A1*) plus three times the SD (Table 3).

$$y = A2 + \frac{A1 - A2}{\left(1 + \left(\frac{x}{x1/2}\right)^p\right)}. \qquad [\mathbf{3}]$$

Data, Materials, and Software Availability. All study data are included in the article and/or supporting information.

Author affiliations: ^{a}Shmunis School of Biomedicine and Cancer Research, George S. Wise Faculty of Life Sciences, Tel Aviv University, Tel Aviv 69978, Israel; ^{b}Department of Chemistry Materials, Bar-Ilan University, Ramat-Gan 5290002, Israel; ^{c}Center for Nanoscience and Nanotechnology, Tel Aviv University, Tel Aviv 69978, Israel; ^{d}Sagol Center for Regenerative Biotechnology, Tel Aviv University, Tel Aviv 69978, Israel; and ^{e}Center for the Physics and Chemistry of Living Systems, Tel Aviv University, Tel Aviv 69978, Israel

1. R. Tero et al., Formation of cell membrane component domains in artificial lipid bilayer. Sci. Rep. 7, 17905 (2017).
2. Y. Zhang, G. J. Narlikar, T. G. Kutateladze, Enzymatic reactions inside biological condensates. J. Mol. Biol. 433, 166624 (2021).
3. A. R. Longstreet, D. T. McQuade, Organic reaction systems: Using microcapsules and microreactors to perform chemical synthesis. Acc. Chem. Res. 46, 327–338 (2013).
4. N. Dammes et al., Conformation-sensitive targeting of lipid nanoparticles for RNA therapeutics. Nat. Nanotechnol. 16, 1030–1038 (2021).
5. N. Krinsky et al., Synthetic cells synthesize therapeutic proteins inside tumors. Adv. Healthc. Mater. 7, e1701163 (2018).
6. Y. Anraku et al., Systemically injectable enzyme-loaded polyion complex vesicles as in vivo nanoreactors functioning in tumors. Angew. Chem. Int. Ed. Engl. 128, 570–575 (2016).
7. A. Lampel, Biology-inspired supramolecular peptide systems. Chem. 6, 1222–1236 (2020).
8. Y. Shen et al., Biomolecular condensates undergo a generic shear-mediated liquid-to-solid transition. Nat. Nanotechnol. 15, 841–847 (2020).
9. C. Yuan et al., Nucleation and growth of amino acid and peptide supramolecular polymers through liquid-liquid phase separation. Angew. Chem. Int. Ed. Engl. 131, 18284–18291 (2019).
10. S. F. Banani, H. O. Lee, A. A. Hyman, M. K. Rosen, Biomolecular condensates: Organizers of cellular biochemistry. Nat. Rev. Mol. Cell Biol. 18, 285–298 (2017).
11. W. M. Aumiller, C. D. Keating, Phosphorylation-mediated RNA/peptide complex coacervation as a model for intracellular liquid organelles. Nat. Chem. 8, 129–137 (2016).
12. L. Faltova, A. M. Küffner, M. Hondele, K. Weis, P. Arosio, Multifunctional protein materials and microreactors using low complexity domains as molecular adhesives. ACS Nano. 12, 9991–9999 (2018).
13. M. Abbas, W. P. Lipiński, J. Wang, E. Spruijt, Peptide-based coacervates as biomimetic protocells. Chem. Soc. Rev. 50, 3690–3705 (2021).
14. S. Roberts et al., Injectable tissue integrating networks from recombinant polypeptides with tunable order. Nat. Mater. 17, 1154–1163 (2018).
15. B. Gabryelczyk et al., Hydrogen bond guidance and aromatic stacking drive liquid-liquid phase separation of intrinsically disordered histidine-rich peptides. Nat. Commun. 10, 5465 (2019).
16. C. Donau et al., Active coacervate droplets as a model for membraneless organelles and protocells. Nat. Commun. 11, 1–10 (2020).
17. B. Drobot et al., Compartmentalised RNA catalysis in membrane-free coacervate protocells. Nat. Commun. 9, 3643 (2018).
18. I. Katzir, E. Haimov, A. Lampel, Tuning the dynamics of viral factories-inspired compartments formed by peptide-RNA liquid-liquid phase separation. Adv. Mater. 34, e2206371 (2022).
19. D. W. P. M. Lowik, E. H. P. Leunissen, M. van den Heuvel, M. B. Hansen, J. C. M. van Hest, Stimulus responsive peptide based materials. Chem. Soc. Rev. 39, 3394–3412 (2010).
20. E. H. Reed, B. S. Schuster, M. C. Good, D. A. Hammer, SPLIT: Stable protein coacervation using a light induced transition. ACS Synth. Biol. 9, 500–507 (2020).
21. A. M. Küffner et al., Acceleration of an enzymatic reaction in liquid phase separated compartments based on intrinsically disordered protein domains. ChemSystemsChem 2, e2000001 (2020).
22. P. A. Riley, Melanogenesis and melanoma. Pigment Cell Res. 16, 548–552 (2003).

23. M. Xiao et al., Stimuli-responsive structurally colored films from bioinspired synthetic melanin nanoparticles. *Chem. Mater.* **28**, 5516–5521 (2016).
24. M. Xiao et al., Bio-inspired structural colors produced via self-assembly of synthetic melanin nanoparticles. *ACS Nano.* **9**, 5454–5460 (2015).
25. T. Massarano, A. Baruch Leshem, M. Weitman, A. Lampel, Spatiotemporal control of melanin synthesis in liquid droplets. *ACS Appl. Mater. Interfaces* **14**, 20520–20527 (2022).
26. C. Wang et al., Skin pigmentation-inspired polydopamine sunscreens. *Adv. Funct. Mater.* **28**, 1802127 (2018).
27. A. Lampel et al., Melanin-inspired chromophoric microparticles composed of polymeric peptide pigments. *Angew. Chem. Int. Ed. Engl.* **60**, 7564–7569 (2021).
28. S. M. M. Reddy et al., Proton-conductive melanin-like fibers through enzymatic oxidation of a self-assembling peptide. *Adv. Mater.* **32**, e2003511 (2020).
29. A. Camus et al., High conductivity Sepia melanin ink films for environmentally benign printed electronics. *Proc. Natl. Acad. Sci. U.S.A.* **119**, e2200058119 (2022).
30. K. Y. Ju, Y. Lee, S. Lee, S. B. Park, J. K. Lee, Bioinspired polymerization of dopamine to generate melanin-like nanoparticles having an excellent free-radical-scavenging property. *Biomacromolecules* **12**, 625–632 (2011).
31. V. Wulf et al., Multicomponent system of single-walled carbon nanotubes functionalized with a melanin-inspired material for optical detection and scavenging of metals. *Adv. Funct. Mater.* **32**, 2209688 (2022).
32. T. Kushimoto et al., A model for melanosome biogenesis based on the purification and analysis of early melanosomes. *Proc. Natl. Acad. Sci. U.S.A.* **98**, 10698–10703 (2001).
33. Y. Huang et al., Mimicking melanosomes: Polydopamine nanoparticles as artificial microparasols. *ACS Cent. Sci.* **3**, 564–569 (2017).
34. M. d'Ischia et al., Melanins and melanogenesis: From pigment cells to human health and technological applications. *Pigment Cell Melanoma Res.* **28**, 520–544 (2015).
35. D. M. Fowler et al., Functional amyloid formation within mammalian tissue. *PLoS Biol.* **4**, 0100–0107 (2006).
36. R. P. McGlinchey et al., The repeat domain of the melanosome fibril protein Pmel17 forms the amyloid core promoting melanin synthesis. *Proc. Natl. Acad. Sci. U.S.A.* **106**, 13731–13736 (2009).
37. M. d'Ischia, A. Napolitano, A. Pezzella, P. Meredith, M. Buehler, Melanin biopolymers: Tailoring chemical complexity for materials design. *Angew. Chem. Int. Ed. Engl.* **59**, 11196–11205 (2020).
38. A. Baruch Leshem et al., Biomolecular condensates formed by designer minimalistic peptides. *Nat. Commun.* **14**, 421 (2023).
39. S. Choi, M. C. O. Meyer, P. C. Bevilacqua, C. D. Keating, Phase-specific RNA accumulation and duplex thermodynamics in multiphase coacervate models for membraneless organelles. *Nat. Chem.* **14**, 1110–1117 (2022).
40. A. Lampel et al., Polymeric peptide pigments with sequence-encoded properties. *Science* **356**, 1064–1068 (2017).
41. K. Deepankumar et al., Liquid-liquid phase separation of the green mussel adhesive protein Pvfp-5 is regulated by the post-translated dopa amino acid. *Adv. Mater.* **34**, 1–10 (2022).
42. Q. Guo et al., Hydrogen-bonds mediate liquid-liquid phase separation of mussel derived adhesive peptides. *Nat. Commun.* **13**, 5771 (2022).
43. M. Abbas, J. O. Law, S. N. Grellscheid, W. T. S. Huck, E. Spruijt, Peptide-based coacervate-core vesicles with semipermeable membranes. *Adv. Mater.* **34**, e2202913 (2022).
44. Y. F. Fan et al., Spectrophotometric assays for sensing tyrosinase activity and their applications. *Biosensors (Basel)* **11**, 290 (2021).
45. L. Panzella, A. Napolitano, Natural and bioinspired phenolic compounds as tyrosinase inhibitors for the treatment of skin hyperpigmentation: Recent advances. *Cosmetics* **6**, 57 (2019).
46. I. F. dos Santos Videira, D. F. L. Moura, S. Magina, Mechanisms regulating melanogenesis. *An. Bras. Dermatol.* **88**, 76 (2013).